

The study on transiting systems HAT-P-13, HAT-P-16 and WASP-32 through combining ground-based and TESS photometry

L. Sun,^{1,2} S. Gu,^{1,2,3} X. Wang,^{1,2,3*} L. Bai,^{1,2,3} J. H. M. M. Schmitt,⁴ V. Perdelwitz,^{5,4} P. Ioannidis⁴

¹Yunnan Observatories, Chinese Academy of Sciences, Kunming 650216, China

²Key Laboratory for the Structure and Evolution of Celestial Objects, Chinese Academy of Sciences, Kunming 650216, China

³School of Astronomy and Space Science, University of Chinese Academy of Sciences, Beijing 101408, China

⁴Hamburger Sternwarte, Universität Hamburg, Gojenbergsweg 112, 21029 Hamburg, Germany

⁵Department of Physics, Ariel University, Ariel 40700, Israel

Accepted XXX. Received YYY; in original form ZZZ

ABSTRACT

High-precision transit photometry supplies ideal opportunities for detecting new exoplanets and characterizing their physical properties, which usually encode valuable information for unveiling the planetary structure, atmosphere and dynamical history. We present revised properties of three transiting systems (i.e., HAT-P-13, HAT-P-16 and WASP-32) through analyzing TESS photometry and ground-based transit observations, which were obtained at the 1m and 2.4m telescopes of Yunnan Observatories, China, and the 1.2m telescope of Hamburg Observatory, Germany, as well as the data in the literature. During modelling the transit light curves, Gaussian process is employed to account for the potential systematic errors. Through comprehensive timing analysis, we find that both HAT-P-13b and HAT-P-16b show significant timing variations (TTVs) that can be explained by apsidal precession. TTVs of WASP-32b may be led by a decaying orbit due to tidal dissipation or apsidal precession. However, the current observations can not rule out the origins of three systems' TTVs from gravitational perturbations of close planetary companions conclusively.

Key words: Planets and satellites: fundamental parameters — planets and satellites: individual : HAT-P-13, HAT-P-16, WASP-32 – techniques: photometric

1 INTRODUCTION

The rapid growth in the number of transiting exoplanets plays a fundamental role in the advance of exoplanetary science, thanks to many dedicated exoplanet survey projects like SuperWASP, HATNet, XO, Kepler, K2, TESS, and so on (Bakos et al. 2004; McCullough et al. 2005; Pollacco et al. 2006; Borucki et al. 2011). High-precision photometry for transit events has become one of the most successful methods for detecting new exoplanets and characterizing the exoplanetary systems. Up to 2022 March 15, transiting exoplanets of 3513 had been discovered and confirmed, which reside in 2645 planetary systems; transiting exoplanets are dominant (i.e., $\sim 70\%$) in the confirmed exoplanet population¹. Furthermore, follow-up observations for known transiting exoplanetary systems could not only refine the parameters of the systems, but also provide excellent opportunities to uncover the structure, atmosphere and dynamical evolution of the planets, which allow us to understand the formation and evolution of planetary systems.

Long-term high-precision photometric monitoring for transit events of known exoplanetary systems is of importance for hunting extra planets and planning new observations. In general, a

single exoplanet transits its host star with a steady orbital period on a time scale of years, on which tidal and general relativity effects have no significant accumulation. But the transit timing variation (TTV; Agol et al. 2005; Holman & Murray 2005), which represents the deviation of transit times from a linear ephemeris, will appear in principle when extra bodies exist in the same system. Due to the relatively longer time scales than the orbital periods, on which the gravitational interactions among the exoplanets work to generate significant TTVs, the space missions, such as *Kepler*, TESS and upcoming PLATO, and ground-based long-term high-precision photometry are more possible to seize such signals (Mazeh et al. 2013; Rowe et al. 2014; Holczer et al. 2016). The overall shapes, amplitudes and frequencies of these TTVs induced by the gravitational interactions, primarily determined by their orbital parameters and masses (see e.g. Agol et al. 2005; Holman & Murray 2005; Nesvorný & Morbidelli 2008; Lithwick et al. 2012; Xie et al. 2014). Therefore, TTV technique is often served as an important tool for characterizing exoplanetary systems: it can supply limits for the hidden exoplanets, hence remedying the absent information on the genuine planetary orbital architectures due to the detection bias inherent to the transit method (Xie et al. 2014; Zhu et al. 2018; Sun et al. 2022), which benefits the study on synthetic planetary system population (see e.g. Mordasini et al. 2009; Mordasini 2018; Wu et al. 2019). In addition,

¹ <http://exoplanet.eu/>

TTV technique is able to weigh the exoplanets in multi-planetary systems (see e.g. Nesvorný et al. 2012; Lithwick et al. 2012), and therefore their densities, which provide tight constraints on their internal structures, such as the analyses for Kepler-411 system (Sun et al. 2019), Trappist-1 system (Grimm et al. 2018) and so on. The discovery of distinct dynamically active systems could also be used to constrain the planetary formation and evolution models, since the present orbital architectures of such systems may hold the imprints from their past orbital migrations (see e.g. Delisle 2017; Nesvorný et al. 2022).

There are some exoplanetary systems exhibiting temporal variations in their orbital periods, however, other origins may cause the change in their orbital periods (Patra et al. 2017; Yee et al. 2020; Turner et al. 2021; Baluev et al. 2019; Bouma et al. 2019, 2020), such as tidal dissipation (Barker & Ogilvie 2010), apsidal precession (Giménez & Bastero 1995), spot crossing events (Sun et al. 2017), planetary mass loss driven by atmospheric escape (Fujita et al. 2022), and so on; these origins would likely imitate the TTV signals originated from gravitational interactions with other planetary bodies. However, orbital decay driven by tidal dissipation is another case deserving for further investigation, in addition to the case of gravitational interactions with other bodies. Such kind of TTV signals could place constraints on the tidal quality factors and experienced dynamical history of the planets (Goldreich & Soter 1966). Associated theory suggests that it is likely to exhibit in massive hot Jupiters.

Here we present TTV analyses on HAT-P-13, HAT-P-16 and WASP-32 planetary systems. Since 2010, we have monitored their transit events using the 1 m and 2.4 m telescopes of Yunnan Observatories (hereafter, YO-1m and YO-2.4m) in China and the 1.2 m Oskar-Lühning telescope (hereafter, OLT-1.2m) at Hamburg Observatory in Germany. As a result, a series of high-precision photometric transit data were obtained. In addition, HAT-P-13, HAT-P-16 and WASP-32 were observed by TESS in sectors 47, 17 and 42, respectively. Furthermore, HAT-P-16 was observed by TESS in Sector 57 (2022 September 30 to 2022 October 29). In this paper, we present the timing analyses of these planetary systems. First, we briefly introduce each target in Section 2. Subsequently, the description for the observations and data reduction strategy are present in Section 3 and 4, respectively. In Section 5 the transit modeling is described. We then discuss the results in Section 6. At last, we summarize the study in Section 7.

2 TARGETS

2.1 HAT-P-13

The multi-planet system HAT-P-13 was discovered by Bakos et al. (2009). This system has a inner transiting hot Jupiter HAT-P-13b and a outer extremely massive planet HAT-P-13c, which orbits a metal-rich ($[Fe/H] = +0.41 \pm 0.08$) host star with periods of 2.9 and 428.5 days, respectively. Winn et al. (2010) found the spin-orbit of this system is well aligned by modeling the Rossiter-McLaughlin (R-M) effect, and evidence for the third companion based on the long term radial acceleration of the host star. Szabó et al. (2010) observed HAT-P-13 system to detect a possible transit of HAT-P-13c by their multi-site campaign, they found HAT-P-13c was most likely not a transiting exoplanet. Moreover, Szabó et al. (2010) obtained two additional transit events and refined the orbital period of HAT-P-13b. Nascimbeni et al. (2011), Pál et al. (2011), Fulton et al. (2011), Payne & Ford (2011), Southworth et al. (2012), Sada & Ramón-Fox (2016), and Baluev et al. (2019) acquired new transiting light curves

of HAT-P-13b based on several ground-based telescopes, refined the physical parameters and analyzed the TTVs. Although the available transit times deviated from a linear ephemeris, the residuals of the transit times were complex rather than expected sinusoid. Turner et al. (2016) observed a transit event of HAT-P-13b in the near-UV, and found the available multi-wavelength photometric transit depths from near-UV to optical wavelengths were not able to well constrain the atmospheric model for HAT-P-13 b due to the large error bars. Kramm et al. (2012) and Batygin et al. (2016) modeled the interior structure of HAT-P-13b using the observationally determined tidal Love number k_2 , then Buhler et al. (2016) and Hardy et al. (2017) imposed constraints on the orbital eccentricity, the tidal Love number k_2 , and the interior structure of HAT-P-13b based on the same set of two secondary-eclipse observations collected by Spitzer Space Telescope.

2.2 HAT-P-16

HAT-P-16b was discovered by Buchhave et al. (2010), which is a massive transiting hot Jupiter (i.e., $M_p = 4.193 \pm 0.094 M_{Jup}$; $R_p = 1.289 \pm 0.066 R_{Jup}$) orbiting a relatively bright ($V=10.8$) F-type host star with a period of 2.7 days. Moutou et al. (2011) studied the R-M effect of HAT-P-16 system, and the projected spin-orbit angle is $\lambda = -10 \pm 16^\circ$. Sada et al. (2012), Ciceri et al. (2013), Pearson et al. (2014), Aladağ et al. (2021) and Wang et al. (2018a) acquired new transiting light curves of HAT-P-16b using several ground-based telescopes, refined the system parameters and found no significant TTV. Davoudi et al. (2020) re-analyzed several relative high quality transit light curves of HAT-P-16b collected from the Exoplanet Transit Database (ETD)². They found that the newly derived physical parameters of HAT-P-13 were in good agreement with those in NASA exoplanet archive.

2.3 WASP-32

WASP-32b is a massive transiting hot Jupiter (i.e., $R_p = 1.190 \pm 0.047 R_{Jup}$; $M_p = 3.59 \pm 0.06 M_{Jup}$), discovered by Maxted et al. (2010) in the SuperWASP survey, orbiting a Sun-like lithium-poor star ($V = 11.3$ mag) every 2.72 days. Sada et al. (2012) obtained one *J*-band transiting light curve of WASP-32 utilizing the Kitt Peak National Observatory's 2.1m telescope and refined the orbital period of the planet. Brown et al. (2012) recalculated the physical parameters of the system and derived a spin-orbit angle of $10^\circ.5^{+6.4}_{-6.5}$ using both the R-M effect and Doppler tomography for WASP-32. Brothwell et al. (2014) confirmed the spin-orbit alignment angle of Brown et al. (2012) utilizing the R-M effect. Sun et al. (2015) recalculated the physical parameters of the system and confirmed no apparent transit timing variation signal for WASP-32. Grauzhanina et al. (2017) found that the intensity and the equivalent width of the H_α line showed a significant change and gave the evidence for WASP-32b filling the Roche lobe and having a comet-like tail based on spectroscopic observations by utilizing the 6m BTA telescope. At last, Valeev et al. (2019) found the presence of Na, K and probable HI based on the transmission spectrum of WASP-32b observed by using 10.4 m GTC telescope.

² <http://var2.astro.cz/ETD/>

3 OBSERVATIONS

3.1 YO-1m photometry

We observed the transit events of HAT-P-13, HAT-P-16 and WASP-32 using the YO-1m telescope (see e.g. Tan et al. 2013; Wang et al. 2013, 2014; Sun et al. 2015, 2017) between 2010 December and 2018 March (see Table 1). The Johnson-Cousins R filter was used during all observations. The 2K×2K CCD camera with a field of view (FOV) of 7.3×7.3 arcmin² was adopted, except on 2017 March 23 when another 4K×4K CCD camera with a FOV of 15×15 arcmin² was utilized. During the observations, the instrument statuses were good, and the exposure times were set according to the weather conditions. Some transit event observations were incomplete, whose light curves had a relatively larger dispersion and/or offset, mostly because the weather rapidly changed to be bad (see Figure 4).

3.2 YO-2.4m photometry

On 2015 November 7, one transit event of WASP-32b was observed by utilizing Yunnan Faint Object Spectrograph and Camera (YFOSC) attached to the YO-2.4m telescope (Fan et al. 2015; Wang et al. 2019) at Yunnan Observatories, China. As YFOSC is not a multi-channel imaging instrument, we obtained nearly simultaneous four-color transit photometry of WASP-32b in Johnson B and V as well as Johnson-Cousins Rc and Ic passbands through rapidly switching the passband filters. The FOV is 9.7×9.7 arcmin². The telescope pointing was maintained using the auto-guiding system, but it was broken down due to a temporal instrument issue during our observation and was reactivated rapidly. The weather was clear with a good seeing. The observing log is listed in Table 1.

3.3 OLT-1.2m photometry

A transit event of HAT-P-16 on 2016 December 8 was observed using an Apogee Alta U9000 CCD camera mounted on the OLT-1.2m telescope at Hamburg Observatory, Germany. The FOV is 9.0×9.0 arcmin². The sky was quite clear and Johnson-Cousins R filter was used in the observation. We used its auto-guiding system during the observation. To improve the photometric precision, the defocusing technique was adopted during the observation. The exposure time was set to 120 s (see Table 1).

3.4 TESS photometry

The TESS spacecraft observed HAT-P-13, HAT-P-16 and WASP-32 during its Sector 47 (2021 December 30 to 2022 January 28), Sector 17 (2019 October 7 to 2019 November 2) and Sector 42 (2021 August 20 to 2021 September 16), respectively. All of the data products with a 2-minute cadence mode reduced by the pipeline created by the Science Processing Operations Center (SPOC; Jenkins et al. 2016) were used in this analysis. The light curve files were retrieved from the archives at Mikulski Archive for Space Telescopes (MAST)³ and the light curves were obtained by employing *Lightkurve* (Lightkurve Collaboration et al. 2018).

4 DATA REDUCTION

4.1 Aperture photometry for ground-based observations

All of CCD images collected by ground-based telescopes were reduced according to the standard procedure as described in Wang et al. (2013), which includes aperture photometry and systematic error correction, and has been integrated into a pipeline. The pipeline was written in Python based on the IRAF package, including image trimming, bias subtraction, flat-field correction and cosmic ray removal. The instrumental magnitudes of the target and reference stars were measured by adopting aperture photometry technique with an optimal aperture, which was to minimize the dispersion of the light curve. The optimal aperture was acquired through comparing the photometric precision for extracted light curves obtained from a series of trial apertures. Then the method proposed by Eastman et al. (2010) was used to convert the observing time into the format of BJD_{TDB} . Because the transit signals of exoplanets are normally shallow, we employed coarse de-correlation (Collier Cameron et al. 2006) and SYSREM algorithms (Tamuz et al. 2005) to diagnose potential systematic errors and correct them so as to enhance the signal-to-noise ratio (SNR) of ground-based transit observations. These systematic errors are mainly due to the extinction of Earth atmosphere, the change of point spread function, the apparent drifts of stars on CCD position associated with the imperfect flat-field correction and so on. In this correction procedure, the least square algorithm was iteratively used to model the patterns of significant systematic errors shared by most reference stars, in which high-quality reference stars with trivial variability was simultaneously identified. We refer interested readers to Wang et al. (2010) for further details. The efficiency of coarse de-correlation (Collier Cameron et al. 2006) and SYSREM (Tamuz et al. 2005) for systematic errors correction would be limited, however, when only several high-quality reference stars were observed in CCD images, whereas other reference stars were much fainter than the target. This issue was apparently presented in the transit observations of HAT-P-13b obtained by employing the 2K×2K CCD camera on YO-1m, because only one reference star has comparable brightness to the target in the FOV. To handle this issue, we employed the Gaussian Process (GP) regression to account for the remaining systematic noises (see 5.1 for details) and eliminated them in photometric data through subtracting the optimal results of GP regression.

5 TRANSIT MODELING

5.1 Initial Transit Modelling

Usually, astronomical photometric data are contaminated by noises, which will reduce the SNR of the signals of interest and hamper the accurate measurements of the physical properties of transiting exoplanets. The correlated components in those noises (i.e., also called systematic noises) are typically associated with instrumental and/or astrophysical sources, such as imperfect flat fielding, variations of the telluric atmosphere, the stellar activity and so on, which cannot generally be eliminated through adopting specific observation technique (Southworth et al. 2009). Therefore, appropriately accounting for the systematic noises by using some noise reduction techniques (see e.g. Collier Cameron et al. 2006; Tamuz et al. 2005; Carter & Winn 2009; Gibson et al. 2012), becomes quite essential in the analysis of the transit observations.

In exoplanet community, a widely adopted way to account for systematic noises is to model them with Gaussian Process (see e.g.

³ <https://archive.stsci.edu/mission/tess/>

Table 1. The observing log of all transit photometry.

No.	Date	Telescope	Target	Exposure time (s)	Number of data points	Duty cycle hour ⁻¹	Filter
1	2013-01-06	YO-1m	HAT-P-13	90	184	36	Rc
2	2013-12-19	YO-1m	HAT-P-13	180	104	19	Rc
3	2014-01-23	YO-1m	HAT-P-13	120	212	27	Rc
4	2014-01-26	YO-1m	HAT-P-13	120	127	27	Rc
5	2014-03-08	YO-1m	HAT-P-13	120	120	27	Rc
6	2014-12-01	YO-1m	HAT-P-13	150	92	22	Rc
7	2015-11-16	YO-1m	HAT-P-13	150	110	22	Rc
8	2016-12-02	YO-1m	HAT-P-13	120	114	27	Rc
9	2017-03-23	YO-1m	HAT-P-13	60	251	51	Rc
10	2018-03-08	YO-1m	HAT-P-13	90	178	36	Rc
11	2010-12-24	YO-1m	HAT-P-16	30	167	90	Rc
12	2011-12-17	YO-1m	HAT-P-16	100	96	33	Rc
13	2016-12-08	OLT-1.2m	HAT-P-16	120	159	28	Rc
14	2015-11-07	YO-2.4m	WASP-32	50	79	26	B
15	2015-11-07	YO-2.4m	WASP-32	30	78	26	V
16	2015-11-07	YO-2.4m	WASP-32	10	78	26	Rc
17	2015-11-07	YO-2.4m	WASP-32	10	78	26	Ic
18	2015-11-18	YO-1m	WASP-32	150	62	22	Rc

Rasmussen & Williams 2006; Gibson et al. 2012; Evans et al. 2015; Hurt et al. 2021; Ahner et al. 2022; Lacedelli et al. 2022). By choosing different forms of the kernel, GPs are able to represent a wide range of signals. Here, we employed publicly available *Juliet* (Espinoza et al. 2019), which is able to model the systematic errors in time series data with GP technique, to diagnose and correct the remaining long-term trends and systematic errors in both TESS and ground-based photometric data.

According to the Gaia DR3 database (Gaia Collaboration et al. 2021), all of our targets are in the relatively evacuated fields and there is no other source bright enough to dilute the transit light curves, so the dilution factors of all targets were fixed to 1 during our transit modelling with *Juliet*. Other fitted transit parameters included the orbital period P (fixed to the optimal values in the literature), the mid-time T_0 , the scaled semi-major axis a/R_A , the eccentricity e (fixed to 0), the argument of periastron ω (fixed to 90 degrees), the impact parameter b , the planet-to-star radius ratio R_p/R_A , the mean out-of-transit flux and the jitter. During modelling the transit light curve, a truncated Gaussian distribution was imposed on the prior of the fitted transit parameter. The centre value and sigma of the Gaussian prior were set to the median and 3 times sigma of its posterior in Bakos et al. (2009) for HAT-P-13, Buchhave et al. (2010) for HAT-P-16 and Maxted et al. (2010) for WASP-32, respectively.

We individually modeled the GPs of each light curve, which were defined for each instrument and observation. We chose the celerite (approximate) Matern multiplied exponential kernel for the GP regression. The hyperparameters of this GP kernel includes the amplitude of the GP, two length scales corresponding to the Matern and the exponential part. Log-uniform priors were imposed for these hyperparameters and the amplitude of the GP varied from 10^{-6} to 10^6 , and both length scales varied from 10^{-3} to 10^3 . We employed the nest sampler *MultiNest* in *Juliet* with 500 live points to explore the parameter space, and obtained optimal systematic error models as well as the transit light curve models of all photometric data sets.

It should be noted that we derived the mid-time of each transit event by modeling each light curve separately with *Juliet* and hence refined the ephemerides. The mid-times of all transit events are listed in Tables 2, 3 and 4. In addition, we collected all available mid-times of these three systems from previous works and the ETD website. A

linear ephemeris formula

$$T_{\text{tra}}(E) = T_0 + P \times E$$

was used to fit all of the mid-times, where T_0 is the zero point, P is the orbital period and E is the orbital cycle number. We employed the Markov Chain Monte Carlo (MCMC) algorithm to fit the mid-times and derived the best-fitting linear ephemeris formula and the orbital period values, respectively. The MCMC algorithm was performed by using the *emcee* package (Foreman-Mackey et al. 2013) and 50,000 MCMC steps with 1,000 burn-in steps was run to ensure the convergence. The final results are

$$T(\text{BJD}_{\text{TDB}} - 2450000) = 4779.92999(33) + 2.9162420(5) \times E$$

for the HAT-P-13 system,

$$T(\text{BJD}_{\text{TDB}} - 2450000) = 5027.59301(19) + 2.7759682(2) \times E$$

for the HAT-P-16 system and

$$T(\text{BJD}_{\text{TDB}} - 2450000) = 5779.06707(24) + 2.7186615(3) \times E$$

for the WASP-32 system.

Finally, we corrected the systematic errors in photometric data through subtracting the optimal results of GP regression from the input light curves. The input light curves with the full median posterior models, the final light curves after the GP correction with the best-fitting deterministic models and the corresponding residuals are presented in Figures 1, 2 and 3.

5.2 Final Transit Modelling

We used the MCMC transit modeling code developed by Collier Cameron et al. (2007) to model the above final light curves simultaneously and derived the system parameters. The free parameters of MCMC code of Collier Cameron et al. (2007) are the orbital period of the transiting exoplanet P , the mid-time of one reference transit event T_0 , the impact parameter b , the transit duration T_{14} , the transit depth ΔF , the semi-amplitude of the radial velocity curve K , the orbital eccentricity e and the argument of periastron ω , respectively. We refer interest reader to Collier Cameron et al. (2007) for further details. The empirical calibration proposed by Enoch et al. (2010) were used to calculate the masses and radii of host stars, which is

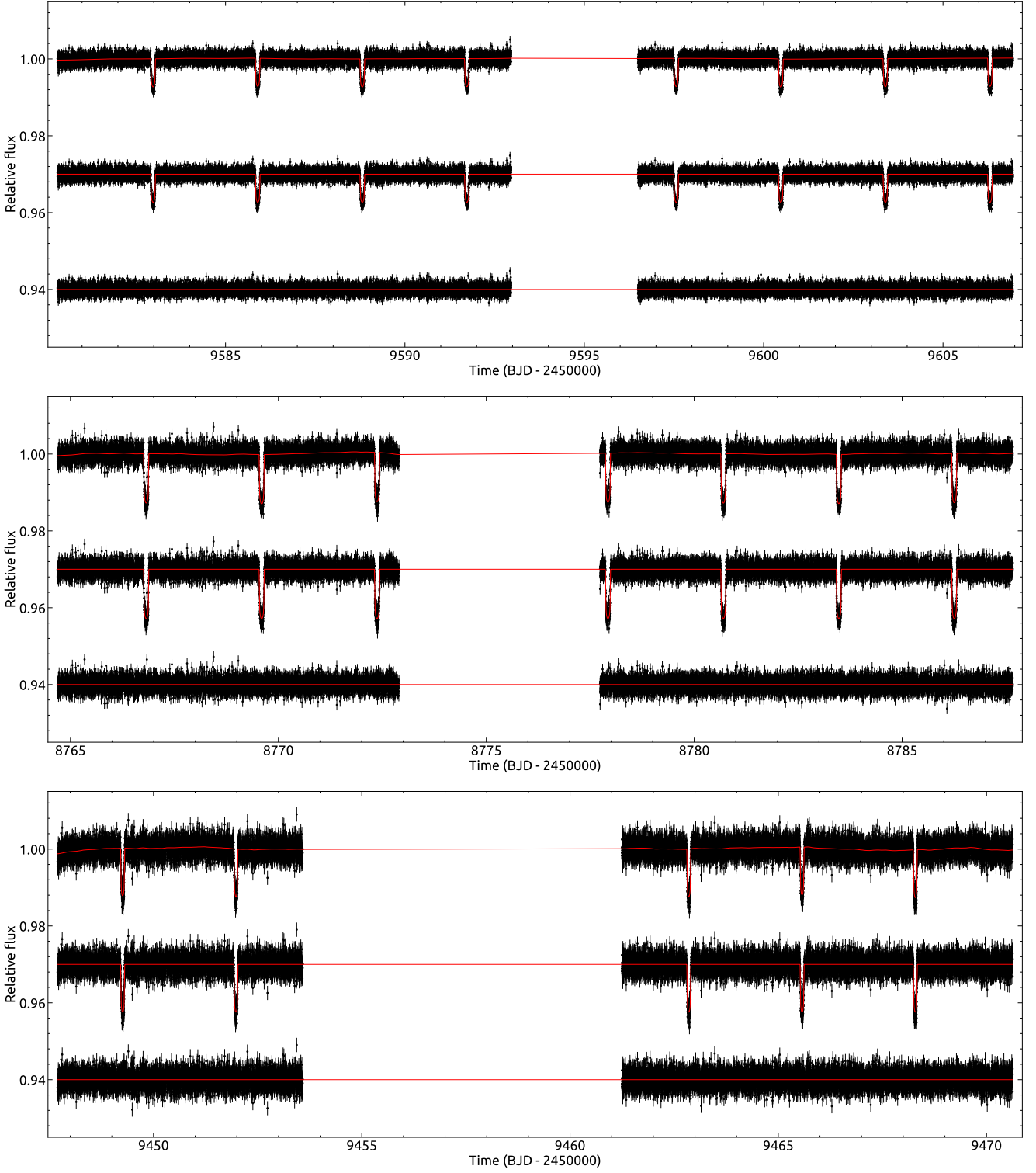


Figure 1. Transit light curves of HAT-P-13 (top panel), HAT-P-16 (middle panel) and WASP-32 (bottom panel) observed by TESS. In each panel, the top is raw light curves with the full median posterior models, the middle is the final light curves with the best-fitting deterministic transit models, and the bottom is the corresponding residuals. Vertical shifts are added for visualization.

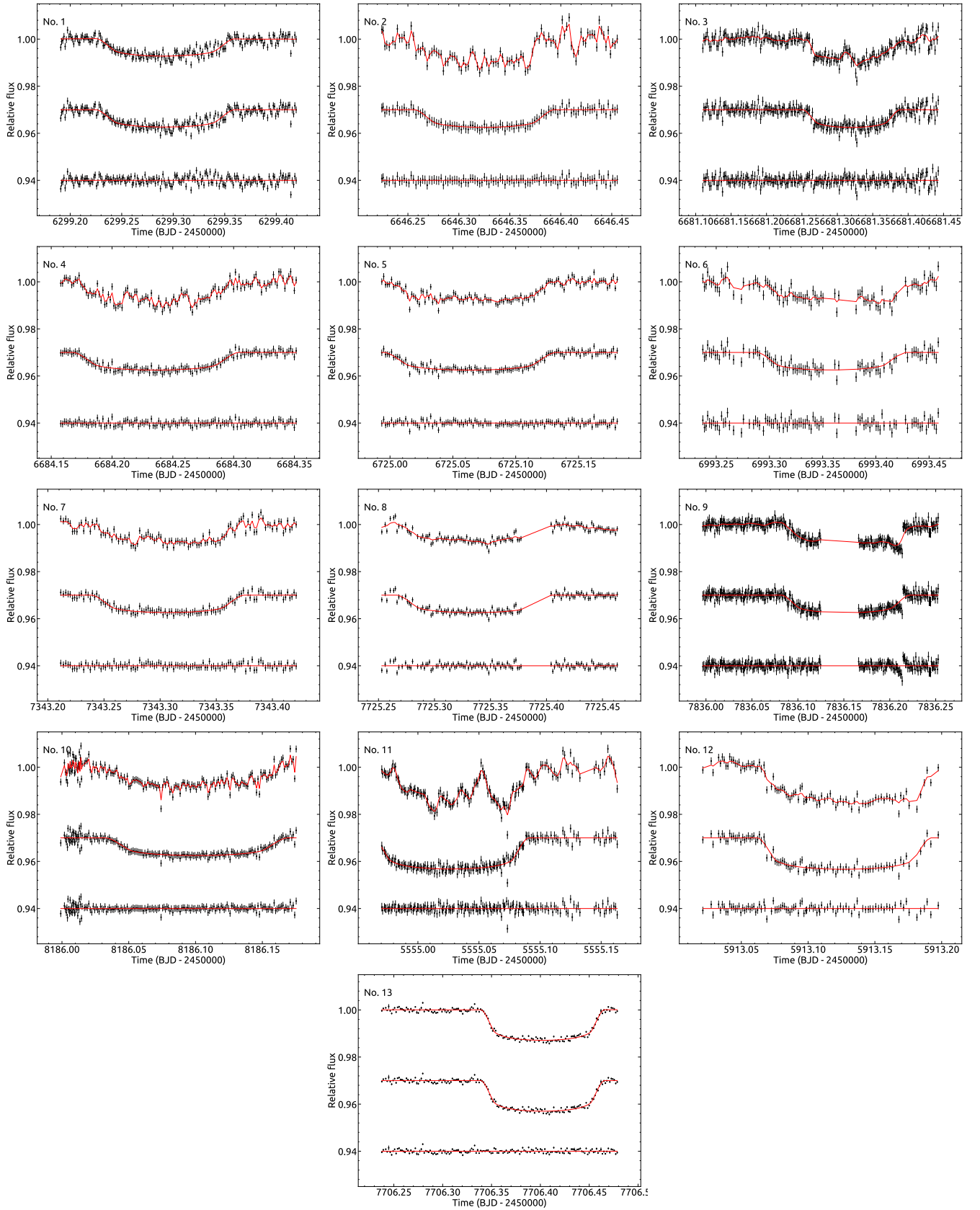


Figure 2. Transit light curves of HAT-P-13 (from No. 1 to 10) and HAT-P-16 (from No. 11 to 13) observed by ground-based telescopes. In each panel, the top is input light curves with the full median posterior models, the middle is the final light curves with the best-fitting deterministic transit models, and the bottom is the corresponding residuals. Vertical shifts are added for visualization.

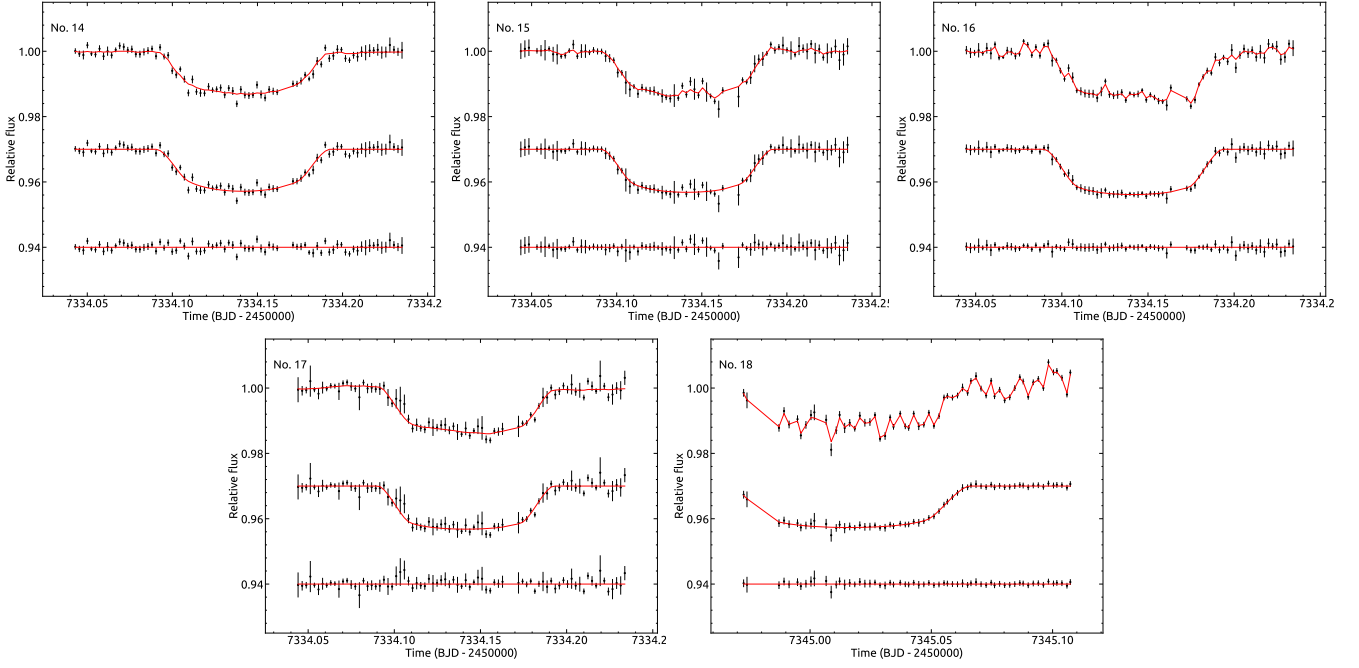


Figure 3. Transit light curves of WASP-32 (from No. 14 to 18) observed by ground-based telescopes. In each panel, the top is input light curves with the full median posterior models, the middle is the final light curves with the best-fitting deterministic transit models, and the bottom is the corresponding residuals. Vertical shifts are added for visualization.

based on the effective temperature, metallicity and mean density of the host star. We obtained the four-coefficient limb-darkening coefficients through interpolating the coefficient tables of [Claret \(2000\)](#) and [Claret \(2004\)](#) based on stellar atmospheric parameters obtained by [Bakos et al. \(2009\)](#), [Buchhave et al. \(2010\)](#) and [Maxted et al. \(2010\)](#). Circular orbits ($e = 0$) were adopted in following analyses, because no significant non-zero eccentricities was found through fitting RV data in the literature.

We calculated the final system parameters of each system through modeling all of the light curves simultaneously for each system by employing the code of [Collier Cameron et al. \(2007\)](#). The refined orbital periods derived in Section 5.1 were fixed in the global modeling. We ran 5 chains of 17,000 MCMC steps with 2,000 burn-in steps as in [Wang et al. \(2013\)](#). We repeated this process for extra ten times to check the convergence of the MCMC sampling, then we obtained consistent results. The final results of the system parameters for each system are listed in Table 5, and the results of discovery papers are also listed there for comparison. Our results are consistent with theirs and have significant improvements. All light curves with best-fitting models and the residuals are shown in Figures 4, 5 and 6.

6 TTV MODELING

6.1 TTV signals

As introduced in Section 1, a few physical processes could stimulate perturbation on hot Jupiter's orbits and/or distort observed transit light curves, for example, spot crossing events, and hence generate measurable TTVs. We considered four scenarios to interpret TTVs of these systems, namely linear ephemeris, orbital decay, apsidal precession and planetary gravitational perturbation. The spot crossing event is not discussed here because of the absence of apparent patterns of spot modulation in TESS light curves. In this subsection,

we firstly modeled observed transit times based on the former three models.

The first model is based on the assumption that the orbital period is a constant as mentioned before,

$$T_{tra}(E) = T_0 + P \times E$$

$$T_{occ}(E) = T_0 + \frac{P}{2} + P \times E$$

, where T_0 is zero point and E is the cycle number, respectively.

The second model assumes that the orbital period is changing with a steady rate (e.g, [Patra et al. 2017](#); [Yee et al. 2020](#); [Turner et al. 2021](#)),

$$T_{tra}(E) = T_0 + P \times E + \frac{1}{2} \frac{dP}{dE} E^2$$

$$T_{occ}(E) = T_0 + \frac{P}{2} + P \times E + \frac{1}{2} \frac{dP}{dE} E^2$$

, where dP/dE denotes the decay rate.

And the third model is based on the assumption that the planetary orbit is slightly eccentric and its argument of pericenter is precessing uniformly over time (e.g, [Patra et al. 2017](#); [Yee et al. 2020](#); [Turner et al. 2021](#)),

$$T_{tra}(E) = T_0 + P_s \times E - \frac{eP_a}{\pi} \cos\omega(E)$$

$$T_{occ}(E) = T_0 + \frac{P_a}{2} + P_s \times E + \frac{eP_a}{\pi} \cos\omega(E)$$

$$\omega(E) = \omega_0 + \frac{d\omega}{dE} E$$

$$P_s = P_a \left(1 - \frac{1}{2\pi} \frac{d\omega}{dE} \right)$$

Table 2. The transit and occultation times of HAT-P-13b.

Event	Mid-time (BJD _{TDB} −2450000)	Error (days)	Cycle	Source	Event	Mid-time (BJD _{TDB} −2450000)	Error (days)	Cycle	Source
tra	4581.62443	0.00122	−68	Bakos et al. (2009)	tra	5602.31068	0.00167	282	Nascimbeni et al. (2011)
tra	4777.01324	0.00100	−1	Bakos et al. (2009)	tra	5613.97390	0.00225	286	Fulton et al. (2011)
tra	4779.92990	0.00063	0	Bakos et al. (2009)	tra	5616.89290	0.00152	287	Fulton et al. (2011)
tra	4782.84394	0.00155	1	Bakos et al. (2009)	tra	5619.80786	0.00134	288	Fulton et al. (2011)
tra	4849.92099	0.00075	24	Bakos et al. (2009)	tra	5622.72289	0.00120	289	Sada & Ramón-Fox (2016)
tra	4882.00078	0.00150	35	Bakos et al. (2009)	tra	5622.72351	0.00166	289	Fulton et al. (2011)
tra	4960.74005	0.00178	62	Bakos et al. (2009)	tra	5669.38140	0.00126	305	Southworth et al. (2012)
tra	5167.79647	0.00280	133	Southworth et al. (2012)	tra	5934.76202	0.00155	396	Sada & Ramón-Fox (2016)
tra	5194.03566	0.00229	142	Fulton et al. (2011)	tra	5978.50418	0.00097	411	ETD
tra	5196.95450	0.00127	143	Fulton et al. (2011)	tra	6299.29216	0.00113	521	This work
tra	5199.86837	0.00123	144	Southworth et al. (2012)	tra	6316.79247	0.00117	527	Sada & Ramón-Fox (2016)
tra	5199.86867	0.00131	144	Fulton et al. (2011)	tra	6351.78519	0.00211	539	Sada & Ramón-Fox (2016)
tra	5231.94542	0.00091	155	Fulton et al. (2011)	tra	6354.69740	0.00140	540	Turner et al. (2016)
tra	5240.69554	0.00197	158	Sada & Ramón-Fox (2016)	tra	6354.70220	0.00112	540	Sada & Ramón-Fox (2016)
tra	5249.45117	0.00200	161	Szabó et al. (2010)	tra	6646.32391	0.00105	640	This work
tra	5269.86567	0.00180	168	Southworth et al. (2012)	tra	6681.32041	0.00127	652	This work
tra	5272.77577	0.00120	169	Southworth et al. (2012)	tra	6684.23580	0.00074	653	This work
tra	5272.77627	0.00250	169	Southworth et al. (2012)	tra	6701.73623	0.00139	659	Sada & Ramón-Fox (2016)
tra	5275.69207	0.00180	170	Southworth et al. (2012)	tra	6725.06439	0.00101	667	This work
tra	5275.69312	0.00266	170	Fulton et al. (2011)	tra	6993.36034	0.00182	759	This work
tra	5307.77077	0.00370	181	Southworth et al. (2012)	tra	7063.35170	0.00125	783	ETD
tra	5310.69197	0.00250	182	Southworth et al. (2012)	tra	7334.55789	0.00085	876	ETD
occ	5326.70818	0.00406	187	Hardy et al. (2017)	tra	7343.30634	0.00088	879	This work
occ	5355.87672	0.00226	197	Hardy et al. (2017)	tra	7725.33461	0.00292	1010	This work
tra	5511.90854	0.00141	251	Fulton et al. (2011)	tra	7754.49545	0.00084	1020	ETD
tra	5558.56302	0.00098	267	Pál et al. (2011)	tra	7827.40114	0.00168	1045	ETD
tra	5561.48416	0.00400	268	Pál et al. (2011)	tra	7836.15281	0.00066	1048	This work
tra	5564.39876	0.00180	269	Nascimbeni et al. (2011)	tra	8186.10079	0.00101	1168	This work
tra	5584.81245	0.00118	276	Sada & Ramón-Fox (2016)	tra	8865.58696	0.00076	1401	ETD
tra	5584.81455	0.00153	276	Southworth et al. (2012)	tra	9582.97959	0.00068	1647	This work
tra	5587.73154	0.00151	277	Sada & Ramón-Fox (2016)	tra	9585.89570	0.00064	1648	This work
tra	5590.64523	0.00179	278	Pál et al. (2011)	tra	9588.81230	0.00063	1649	This work
tra	5593.55879	0.00185	279	Southworth et al. (2012)	tra	9591.72847	0.00064	1650	This work
tra	5593.56147	0.00115	279	Nascimbeni et al. (2011)	tra	9597.56058	0.00067	1652	This work
tra	5596.47291	0.00140	280	Southworth et al. (2012)	tra	9600.47816	0.00067	1653	This work
tra	5596.47327	0.00202	280	Southworth et al. (2012)	tra	9603.39419	0.00064	1654	This work
tra	5596.47662	0.00305	280	Nascimbeni et al. (2011)	tra	9606.31091	0.00061	1655	This work
tra	5599.39267	0.00075	281	Nascimbeni et al. (2011)	tra	9253.44747	0.00118	1534	ETD
tra	5599.39446	0.00100	281	Southworth et al. (2012)					

where P_s is the sidereal period, P_a is the anomalistic period, e is the orbital eccentricity, ω is the argument of pericenter and $d\omega/dE$ is the precession rate (Giménez & Bastero 1995), respectively. We employed the MCMC sampler *emcee* to fit TTV signals based on these three assumptions and obtained the optimal parameters and uncertainties (Foreman-Mackey et al. 2013). In the MCMC sampling, 50000 MCMC samples with 1000 burn-in ones was taken to ensure the convergence. The results of fitted parameters with relative uncertainties are listed in Table 6, and TTVs of these systems with the optimal orbital decay and apsidal precession models are shown in Figures 7, 8 and 9, respectively.

To make a comparison between the alternative models, the Bayesian Information Criterion (BIC; Schwarz 1978) is often adopted. BIC is parameterized as

$$\text{BIC} = \chi^2 + k \log n$$

, where k denotes the number of free parameters and n represents the number of data points.

6.1.1 HAT-P-13

As shown in Figure 7, the transit and occultation times were modelled simultaneously using the procedure mentioned in 6.1. The apsidal precession model has a lower chi-square (i.e., $\chi^2_{\min} = 171.827$) and its BIC value is also the smallest, compared with the constant period model (i.e., $\chi^2_{\min} = 210.947$) and the orbital decay model (i.e., $\chi^2_{\min} = 208.062$). The apsidal precession model is more favored than other two models with $\Delta(\text{BIC}_{3,1}) = 26.089$ and $\Delta(\text{BIC}_{3,2}) = 27.547$. Bayes factors are $B_{3,1} = 4.63 \times 10^5$ and $B_{3,2} = 9.59 \times 10^5$, respectively, which suggests that observed TTV signal significantly supports the apsidal precession model. However, as shown in Figure 7, the apsidal precession model could not well reproduce the observed TTV, in particular the spike signals on some epochs, which possibly suggests that TTV of HAT-P-13 is originated from the orbital perturbations of close companion(s).

Table 3. The transit times of HAT-P-16b.

Event	Mid-time (BJD _{TDB} −2450000)	Error (days)	Cycle	Source	Event	Mid-time (BJD _{TDB} −2450000)	Error (days)	Cycle	Source
tra	5027.59293	0.00031	0	Ciceri et al. (2013)	tra	7642.55557	0.00062	942	ETD
tra	5085.88780	0.00049	21	Ciceri et al. (2013)	tra	7692.52421	0.00092	960	ETD
tra	5085.88864	0.00006	21	Wang et al. (2018a)	tra	7706.40229	0.00032	965	This work
tra	5096.99125	0.00009	25	Wang et al. (2018a)	tra	7706.40419	0.00087	965	ETD
tra	5124.75086	0.00009	35	Wang et al. (2018a)	tra	7773.02393	0.00014	989	Wang et al. (2018a)
tra	5135.85362	0.00050	39	Ciceri et al. (2013)	tra	8036.74082	0.00068	1084	ETD
tra	5135.85449	0.00006	39	Wang et al. (2018a)	tra	8350.42812	0.00062	1197	ETD
tra	5463.41931	0.00080	157	ETD	tra	8375.41142	0.00063	1206	ETD
tra	5463.42067	0.00049	157	ETD	tra	8475.34489	0.00082	1242	ETD
tra	5471.74748	0.00047	160	Sada & Ramón-Fox (2016)	tra	8733.51150	0.00073	1335	ETD
tra	5482.85087	0.00066	164	ETD	tra	8747.38887	0.00074	1340	ETD
tra	5485.62913	0.00050	165	ETD	tra	8766.82141	0.00041	1347	This work
tra	5499.50837	0.00019	170	Ciceri et al. (2013)	tra	8769.59792	0.00046	1348	This work
tra	5555.02710	0.00063	190	This work	tra	8772.37361	0.00043	1349	This work
tra	5796.53707	0.00034	277	Ciceri et al. (2013)	tra	8777.92488	0.00046	1351	This work
tra	5829.84931	0.00059	289	ETD	tra	8780.70199	0.00040	1352	This work
tra	5835.40206	0.00091	291	ETD	tra	8780.70211	0.00068	1352	ETD
tra	5843.72852	0.00081	294	ETD	tra	8783.47734	0.00041	1353	This work
tra	5893.69673	0.00065	312	Sada & Ramón-Fox (2016)	tra	8786.25400	0.00042	1354	This work
tra	5913.12765	0.00087	319	This work	tra	8797.35862	0.00103	1358	Aladağ et al. (2021)
tra	6190.72516	0.00059	419	Sada & Ramón-Fox (2016)	tra	8811.24399	0.00147	1363	Aladağ et al. (2021)
tra	6204.60421	0.00032	424	Ciceri et al. (2013)	tra	8822.34086	0.00055	1367	ETD
tra	6204.60451	0.00030	424	Ciceri et al. (2013)	tra	8836.22609	0.00123	1372	Aladağ et al. (2021)
tra	6226.81172	0.00057	432	ETD	tra	9055.52400	0.00069	1451	ETD
tra	6540.49484	0.00054	545	ETD	tra	9105.49026	0.00049	1469	ETD
tra	6573.80636	0.00057	557	Sada & Ramón-Fox (2016)	tra	9130.47387	0.00066	1478	ETD
tra	6598.79110	0.00060	566	Turner et al. (2016)	tra	9130.47461	0.00052	1478	Aladağ et al. (2021)
tra	6598.79150	0.00079	566	ETD	tra	9144.34689	0.00076	1483	Aladağ et al. (2021)
tra	6601.56852	0.00066	567	ETD	tra	9155.45802	0.00062	1487	ETD
tra	6604.34400	0.00084	568	ETD	tra	9491.34883	0.00073	1608	ETD
tra	7259.47015	0.00099	804	ETD	tra	9541.31793	0.00044	1626	ETD
tra	7334.42244	0.00078	831	ETD	tra	9552.42074	0.00060	1630	ETD
tra	7345.52642	0.00095	835	ETD	tra	9566.29983	0.00072	1635	ETD

Table 4. The transit times of WASP-32.

Event	Mid-time (BJD _{TDB} − 2450000)	Error (days)	Cycle	Source
tra	5496.32648	0.00101	-104	ETD
tra	5507.19973	0.00074	-100	Sun et al. (2015)
tra	5803.53497	0.00072	9	ETD
tra	5803.53506	0.00076	9	ETD
tra	5849.75088	0.00069	26	Sada et al. (2012)
tra	6252.11417	0.00139	174	Sun et al. (2015)
tra	7331.42313	0.00033	571	ETD
tra	7334.14167	0.00019	572	This work
tra	7345.01634	0.00069	576	This work
tra	7619.60135	0.00097	677	ETD
tra	7668.53409	0.00134	695	ETD
tra	8731.53383	0.00074	1086	ETD
tra	9449.25924	0.00061	1350	This work
tra	9451.97865	0.00059	1351	This work
tra	9462.85368	0.00061	1355	This work
tra	9465.57222	0.00071	1356	This work
tra	9468.28993	0.00058	1357	This work

6.1.2 HAT-P-16

As shown in Figure 8, the transit times of HAT-P-16b show significant TTV signal, which deviates from the constant period model with $\chi^2_{min} = 1033.220$ for the degree of freedom of 61. Comparing with

the constant period model, we found that the transit times of HAT-P-16 are favored the orbital decay model ($\chi^2_{min} = 863.871$) and the apsidal precession model ($\chi^2_{min} = 703.054$). Because several transit times obtained by Aladağ et al. (2021) significantly deviates from other TTV measurements, they are eliminated in the TTV modelling process. The apsidal precession model has the lowest BIC value with $\Delta(\text{BIC}_{3,1}) = 317.737$ and $\Delta(\text{BIC}_{3,2}) = 152.532$. This means a predominant interpretation of the apsidal precession model to the observed TTV signal of HAT-P-16. Even if the apsidal model is preferred by BIC, a reduced χ^2 of much large than 10 may imply that the model is possible wrong and/ or the errors of some transit times are underestimated.

6.1.3 WASP-32

As shown in Figure 9, compared with the constant period model (i.e., $\chi^2_{min} = 17.981$) and the apsidal precession model (i.e., $\chi^2_{min} = 13.949$), the orbital decay model fits the timing data of WASP-32 better (i.e., $\chi^2_{min} = 12.217$) and also has smaller BIC value. The orbital decay model is the superior one for interpreting the TTV of WASP-32 with $\Delta(\text{BIC}_{2,1}) = 2.931$ and $\Delta(\text{BIC}_{2,3}) = 7.399$, which means that the observations of WASP-32 slightly favour the orbital decay model.

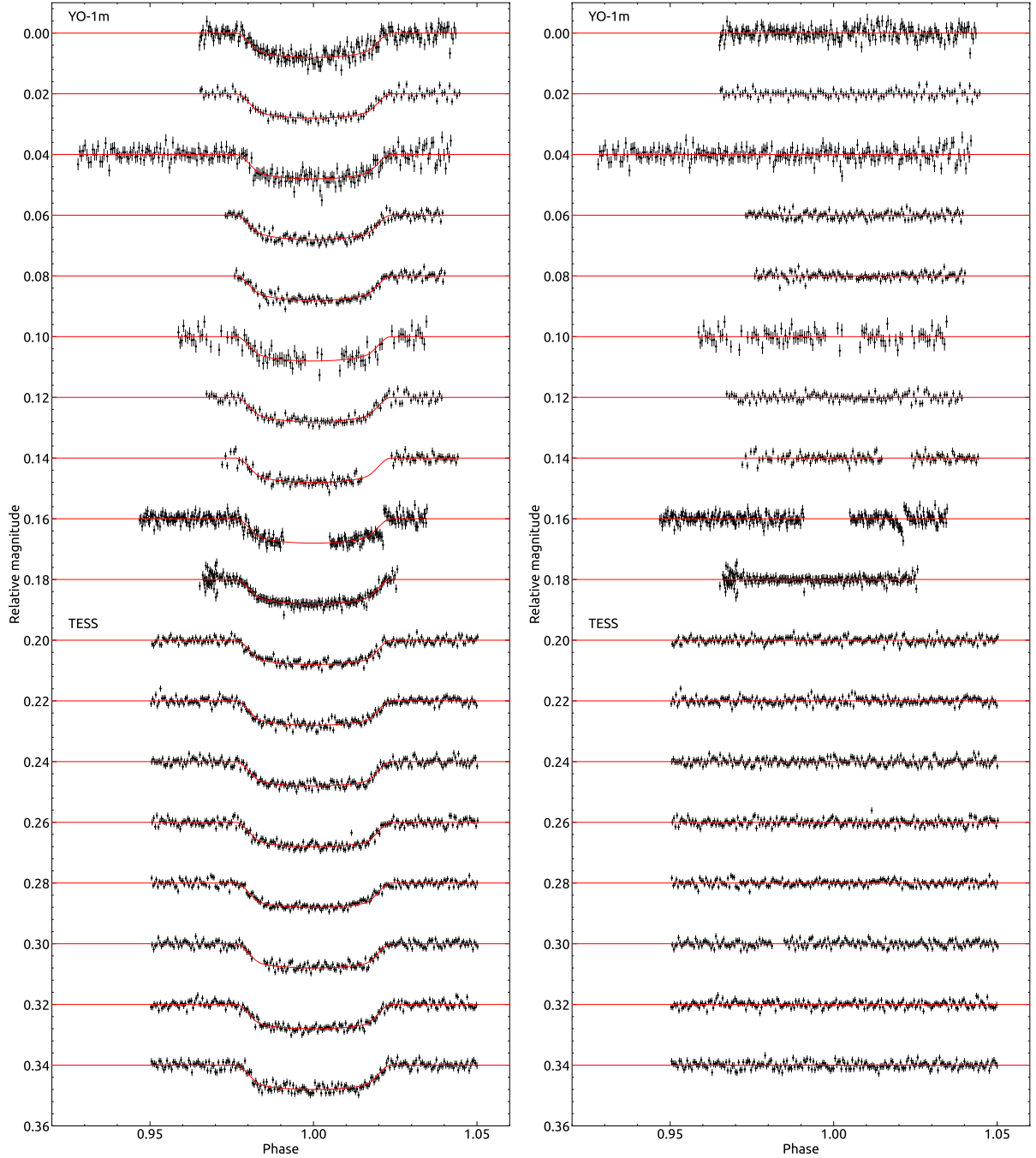


Figure 4. The final transit light curves of HAT-P-13 with the best-fitting transit models and the residuals.

6.2 Upper Mass Limit of a Hypothetical Perturber

TTV signals of transiting exoplanetary systems provide an opportunity to constrain masses of additional perturbing planets, given that these TTVs are triggered by the gravitational perturbation from other planets. While inverting TTV signals has succeeded in detecting new exoplanets (e.g., [Sun et al. 2019](#)), this technique cannot be utilised directly to these three systems, because only TTV measurements with enough high cadence, high SNR and even long observation baseline, like some TTV measurements collected by *Kepler*, may well constrain the orbital period and orbital architecture of the perturber. However, we could utilise the RMS of the TTVs for the sparse

measurements to approximate estimate the property and orbital parameter of extra planets. Before conducting the N -body simulation, we computed the generalised Lomb-Scargle (GLS) periodograms of these three systems' TTVs to search for potential periodic signals ([Zechmeister & Kürster 2009](#)). As a result, we found that the measured TTVs of HAT-P-13b and HAT-P-16b exhibited significant periodic signals. The GLS periodograms and the optimal sine curve fittings for the TTVs of those two system are showed in [10](#) and [11](#), respectively.

In order to constrain the property and orbital parameter of additional planets, we employed a N -body code to perform direct orbit

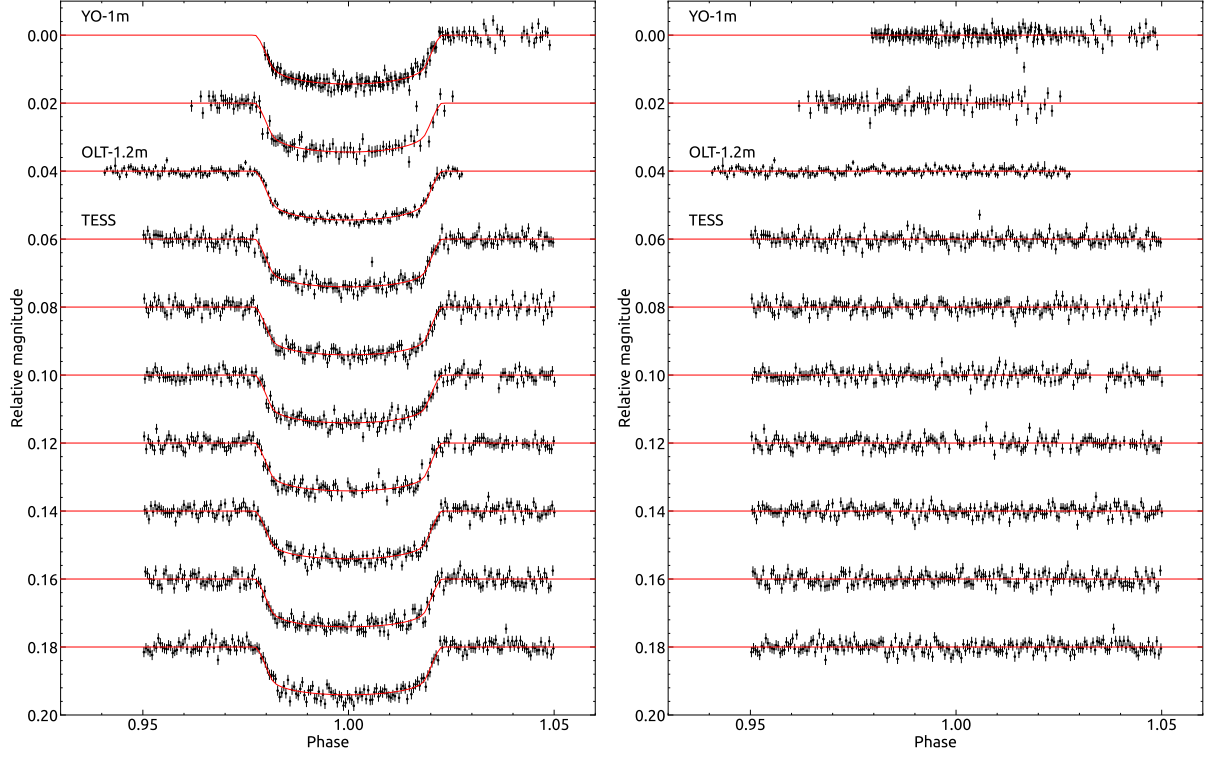


Figure 5. The final transit light curves of HAT-P-16 with the best-fitting transit models and the residuals.

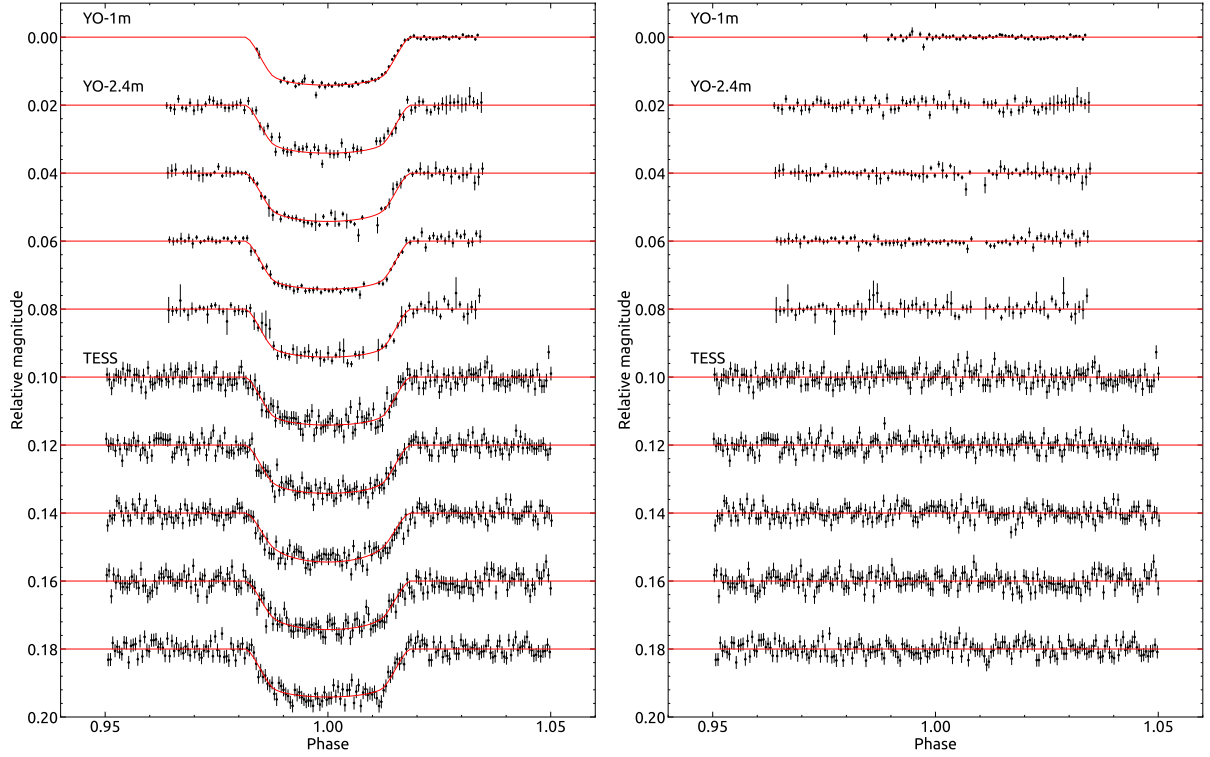


Figure 6. The final transit light curves of WASP-32 with the best-fitting transit models and the residuals.

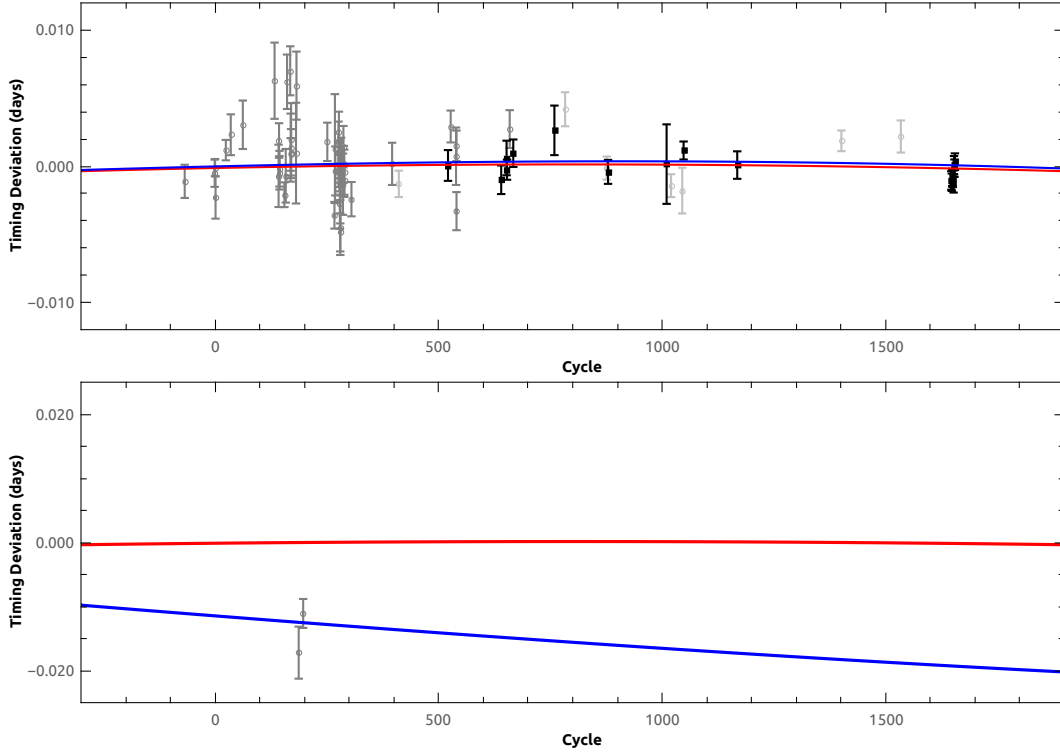


Figure 7. Upper panel: transit timing variation after subtracting the constant-period model of HAT-P-13. The black squares are the new transit times from TESS and our ground-based photometry, the dark gray dots are from the data of previous works, and the light gray ones denote those from ETD; Lower panel: secondary eclipse times variation after subtracting the constant-period model. The red curve shows the expected orbital decay model and the blue curve shows the apsidal precession model.

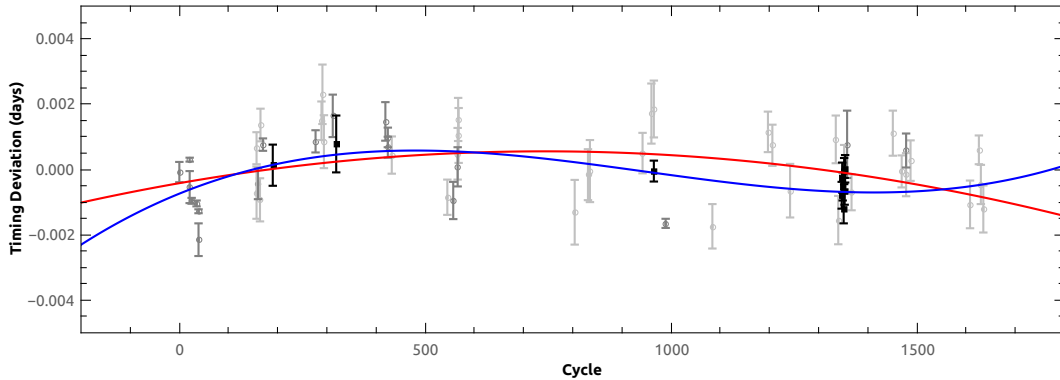


Figure 8. Transit timing variation after subtracting the constant-period model of HAT-P-16. The black squares are the new transit times from TESS and our ground-based photometry, the dark gray dots are from the data of previous works, and the light gray ones denote those from ETD. The red curve shows the expected orbital decay model and the blue curve shows the apsidal precession model.

integration, which was also used in the literature (e.g., Wang et al. 2017, 2018b,a, 2021; Cortés-Zuleta et al. 2020; Bai et al. 2022). In principle, we numerically integrated the orbits of each system with a hypothetic perturbing planet in the system and compared the RMS of their TTVs with the observed. We employed similar methodology as described in Bai et al. (2022) to acquire the upper mass limits.

During integrating the orbits of each system, a large number of trial orbital periods for the perturbing planet was sampled while the other orbital parameters were fixed to specific values. Because TTV signals are dominated by the perturber’s mass, the orbital period, the eccentricity and the mutual inclination of the orbit (Agol et al.

2005; Holman & Murray 2005; Nesvorný & Morbidelli 2008), we considered three different orbital architectures for hypothetical perturbers as a brief demonstration in the following : (a) all planets on coplanar and circular orbits initially; (b) the perturbing planet on a coplanar and slightly eccentric orbit initially (i.e., $e_c = 0.1$); and (c) the perturbing planet on an inclined and slightly eccentric orbit initially (i.e., $i_c = i_b - 30^\circ$, $e_c = 0.1$, where i_b and i_c are the inclinations of the known hot jupiter and the perturber, respectively). Hereafter, these orbital architectures are respectively referred to Case a, Case b and Case c. With the exception of the orbital period of the perturbing planet, the other parameters adopted selected values;

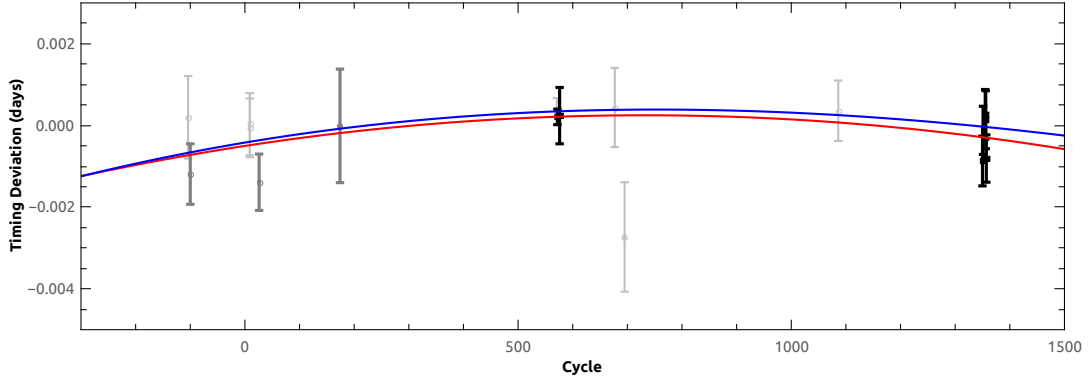


Figure 9. Transit timing variation after subtracting the constant-period model of WASP-32. The black squares are the new transit times from TESS and our ground-based photometry, the dark gray dots are from the data of previous works, and the light gray ones denote those from ETD. The red curve shows the expected orbital decay model and the blue curve shows the apsidal precession model.

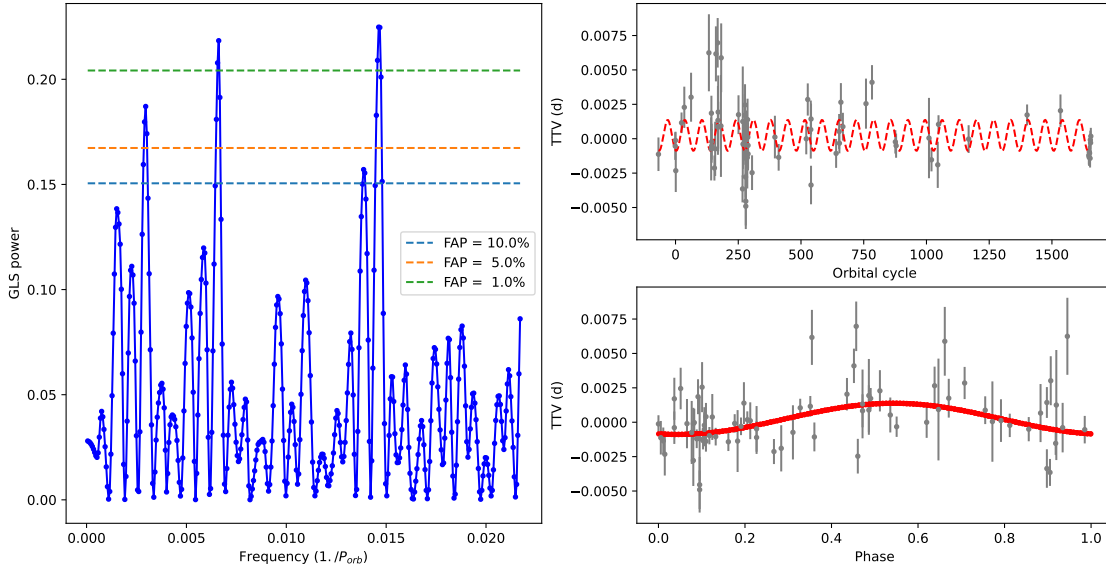


Figure 10. The GLS periodogram of HAT-P-13b' TTV and the optimal sine curve fitting associated with the largest GLS power.

the orbital period of the perturber P_c was uniformly-spaced sampled from 1 day to $10P_b$ with a step of 0.001 days.

Furthermore, the radial velocities (RVs) of the host star generated by a hypothetical perturber would supply extra constraints on the property of the perturber. Given that the planets are not locked in orbital resonance, the RVs of the host star could be represented as the sum of the RVs induced by each planetary component's Keplerian motion (Ford 2006). Therefore, the residuals of RVs after eliminating the components from known transiting planets, would in principle stem from additional bodies. High precision RV measurements with a good coverage in its orbital phase will be required for providing constraints on the orbital period and mass of the perturbing planet. Here we utilized RMS of residuals of each planet's RVs instead of residuals to statistically place constraints on the mass for the hypothetical perturbers. The amplitude K of RV curves induced by a planet on its

host star is represented :

$$\left(\frac{M_p \sin i_p}{M_\oplus} \right) = 11.19 \left(\frac{K}{m/s} \right) \sqrt{1 - e^2} \left(\frac{M_*}{M_\odot} \right)^{2/3} \left(\frac{P_{orb}}{1yr} \right)^{1/3}$$

where P_{orb} , M_p and M_* denote the orbital period of the planet, the mass of the planet and the mass of the host star, respectively. Given that the orbital eccentricities of $e_c \leq 0.1$ for the perturber, the RMS of RV curve statistically equals $\sqrt{2}/2$ times of its amplitude. The mass limits of the hypothetical perturbers are plotted with the yellow curves in Figures 12, 13 and 14 based on the RMS of HAT-P-13, HAT-P-16 and WASP-32's RV residuals.

Extra constraints could also be imposed on the property of the perturber due to the requirement of the stability for the long-run orbital evolution of planetary system. We compute the Mean Exponential Growth factor of Nearby Orbits (MEGNO; Cincotta & Simó 2000; Goździewski et al. 2001; Cincotta et al. 2003) to meet our purpose by utilising REBOUND to numerically integrate the orbits

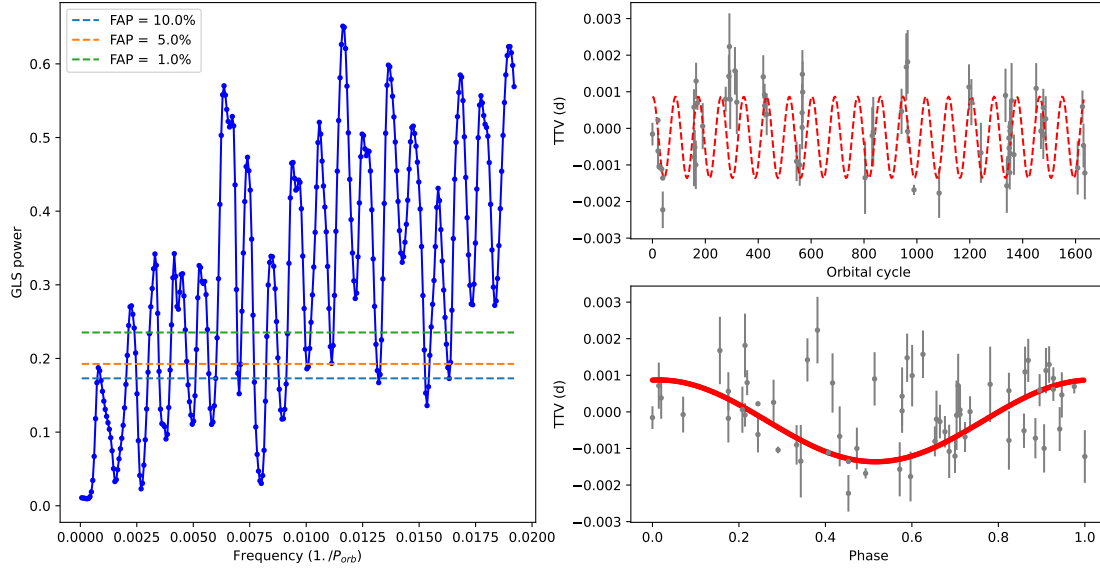


Figure 11. The GLS periodogram of HAT-P-16b' TTV and the optimal sine curve fitting associated with the largest GLS power.

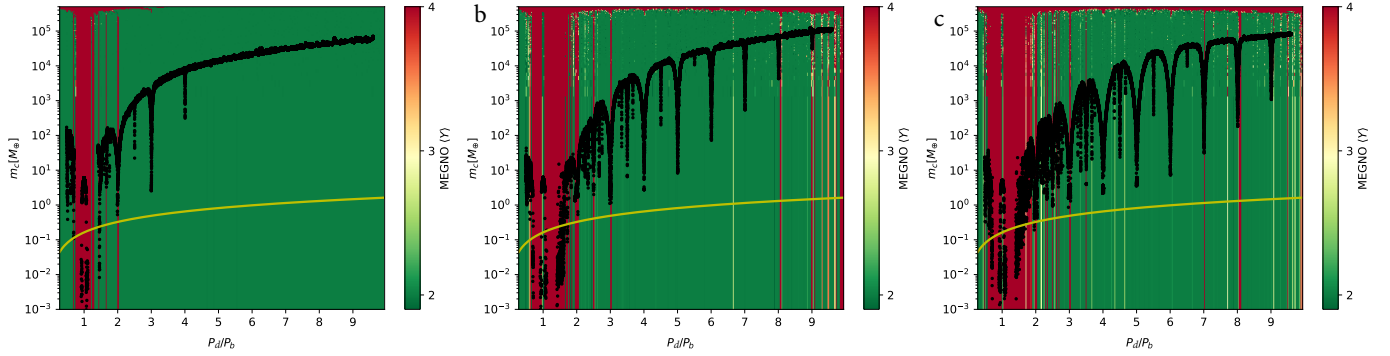


Figure 12. The MEGNO maps of HAT-P-13 based on three different initial conditions. Panel a: the perturber initially on coplanar, circular orbit. Panel b: the perturber initially on coplanar, slightly eccentric orbit ($e = 0.1$). Panel c: the perturber initially on inclined, slightly eccentric orbit ($e = 0.1$). The black scatters are the upper mass limit derived from the RMS of HAT-P-13b's TTVs, while the yellow line is from the constraints of RMS of HAT-P-13's RV residuals after eliminating the components of HAT-P-13 b & c. The parameter spaces for regular orbital architectures color-coded with green are separated from the chaotic ones on the MEGNO maps.

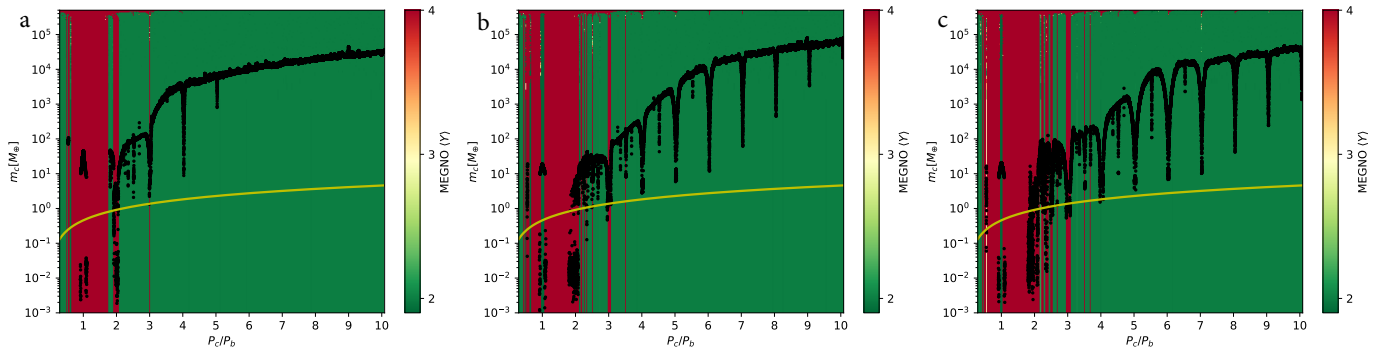


Figure 13. The MEGNO maps of HAT-P-16 based on three different initial conditions. All labels are identical to those in Figure 12.

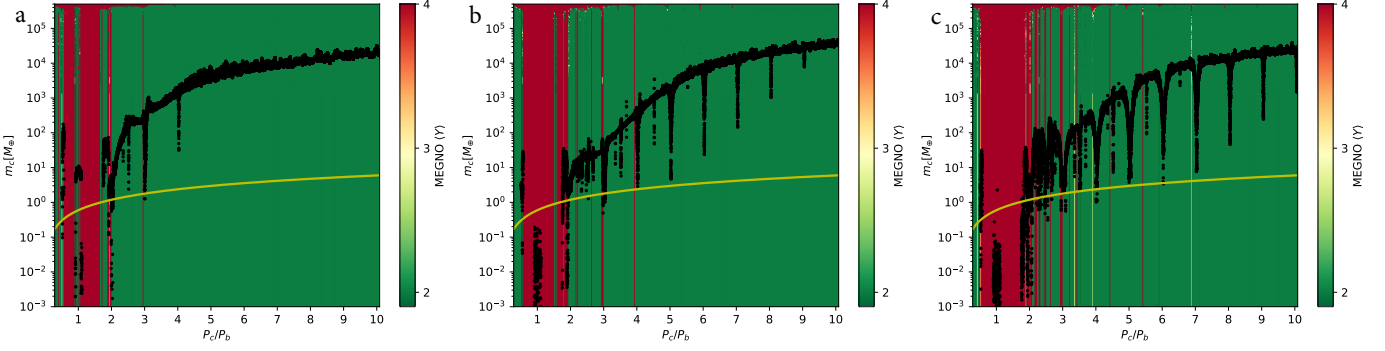


Figure 14. The MEGNO maps of WASP-32 based on three different initial conditions. All labels are identical to those in Figure.12.

Table 5. System parameters of HAT-P-13, HAT-P-16 and WASP-32.

Target	Parameter	Bakos et al. (2009)	This work
HAT-P-13	Orbital period (days)	2.916260±0.000010	2.9162420±0.0000005
	Transit epoch (BJD-2450000)	4779.92979±0.00038	4779.92999±0.00033
	Transit Duration (days)	0.1345±0.0017	0.1344±0.0009
	Planet/star area ratio	0.0071±0.0002	0.0071±0.0001
	Impact parameter	0.668 ^{+0.032} _{-0.045}	0.711±0.002
	Orbital separation (AU)	0.0427 ^{+0.0006} _{-0.0012}	0.0418±0.0003
	Orbital inclination (deg)	83.4±0.6	82.77±0.33
	Orbital eccentricity	0.021±0.009	0 (fixed)
	Stellar radius (R_{\odot})	1.56±0.08	1.590±0.042
	Planet radius (R_{Jup})	1.281±0.079	1.306±0.042
	Stellar effective temperature (K)	5653±90	5651±93
	Planet temperature (K)	1653±45	1681±34
Target	Parameter	Buchhave et al. (2010)	This work
HAT-P-16	Orbital period (days)	2.775960±0.000003	2.7759682±0.0000002
	Transit epoch (BJD-2450000)	5027.59293±0.00031	5027.59301±0.00019
	Transit Duration (days)	0.1276±0.0013	0.1257±0.0006
	Planet/star area ratio	0.0115±0.0002	0.0112±0.0001
	Impact parameter	0.439 ^{+0.065} _{-0.098}	0.272±0.008
	Orbital separation (AU)	0.0413±0.0004	0.0405±0.0002
	Orbital inclination (deg)	86.6±0.7	87.93±0.62
	Orbital eccentricity	0.036±0.004	0 (fixed)
	Stellar radius (R_{\odot})	1.237±0.054	1.157±0.030
	Planet radius (R_{Jup})	1.289±0.066	1.194±0.037
	Stellar effective temperature (K)	6158±80	6158±79
	Planet temperature (K)	1626±40	1587±26
Target	Parameter	Maxted et al. (2010)	This work
WASP-32	Orbital period (days)	2.718659±0.000008	2.7186615 ±0.0000003
	Transit epoch (BJD-2450000)	5151.0546±0.0005	5779.06707 ±0.00024
	Transit Duration (days)	0.101±0.002	0.0999±0.0006
	Planet/star area ratio	0.0124±0.0004	0.0124±0.0001
	Impact parameter	0.64±0.04	0.682±0.014
	Orbital separation (AU)	0.0394±0.0003	0.0394±0.0003
	Orbital inclination (deg)	85.3±0.5	84.85±0.21
	Orbital eccentricity	0.0180±0.0065	0 (fixed)
	Stellar radius (R_{\odot})	1.11±0.05	1.114±0.023
	Planet radius (R_{Jup})	1.18±0.07	1.209±0.031
	Stellar effective temperature (K)	6100±100	6104±103
	Planet temperature (K)	1560±50	1565±30

and simultaneously calculate associated variational equations of motion over a large number of initial orbital states (Rein & Tamayo 2015, 2016). During the simulation, the orbital period and the mass of the purterber were varied; each initial grid based on previously mentioned orbital architectures was integrated for 500 yrs, which would be helpful for finding the location of weak chaotic high-order

mean-motion resonances. MEGNO is widely employed to quantitatively estimate the stochastic behaviour for a non-linear dynamical system and thus capture the chaotic resonances (Goździewski et al. 2001; Hinse et al. 2010). For an initial orbital state, once the chaotic behavior was seized by MEGNO, there is no doubt about its erratic nature in the future (Hins et al. 2010).

Table 6. Timing model parameters of HAT-P-13, HAT-P-16 and WASP-32.

Parameter	HAT-P-13	HAT-P-16	WASP-32
<i>Constant period model</i>			
P (days)	2.9162420 ± 0.0000005	2.7759682 ± 0.0000002	2.7186615 ± 0.0000003
T_0 (BJD-2450000)	4779.92999 ± 0.00033	5027.59301 ± 0.00019	5779.06707 ± 0.00023
N_{dof}	75	61	18
χ^2_{min}	210.947	1033.220	17.981
BIC	219.635	1041.506	23.647
<i>Orbital decay model</i>			
P (days)	2.9162427 ± 0.0000017	2.7759708 ± 0.0000009	2.7186636 ± 0.0000009
T_0 (BJD-2450000)	4779.92987 ± 0.00046	5027.59259 ± 0.00023	5779.06657 ± 0.00031
dP/dE (days/orbit)	$(-0.823 \pm 2.109) \times 10^{-9}$	$(-3.536 \pm 1.212) \times 10^{-9}$	$(-2.806 \pm 1.156) \times 10^{-9}$
N_{dof}	74	60	17
χ^2_{min}	208.062	863.871	12.217
BIC	221.093	876.301	20.716
<i>Apsidal precession model</i>			
P_s (days)	2.9162397 ± 0.0000011	2.7759926 ± 0.0000091	2.7186701 ± 0.0000031
T_0 (BJD-2450000)	4779.92426 ± 0.00106	5027.56989 ± 0.00788	5779.04116 ± 0.01074
e	0.01145 ± 0.00280	0.03503 ± 0.01658	0.03577 ± 0.01493
ω_0 (rad)	2.139 ± 0.107	3.904 ± 0.126	3.744 ± 0.147
$d\omega/dE$ (rad/orbit)	0.00035 ± 0.00019	0.00085 ± 0.00015	0.00036 ± 0.00012
N_{dof}	72	58	15
χ^2_{min}	171.827	703.054	13.949
BIC	193.546	723.769	28.115

In the following subsections, the MEGNO results for each system are presented. For each case, we found the common unstable regions were in the vicinity of the transiting planet labeled as yellow and/or red in MEGNO maps (corresponding to $\langle Y \rangle > 3.5$).

6.2.1 HAT-P-13b

We obtained comparable results to those of Agol et al. (2005) and Holman & Murray (2005), which implies that TTVs are amplified when the orbital architectures are in or near mean motion resonances (hereafter, MMR). In addition, TTV_{RMS} of both Case b and c are far more complex than that in Case a, in which high-order MMRs (e.g., $P_c/P_b \approx 5:1, 6:1$ and so on.) trigger large TTV signals and thus the relative upper mass limit drops rapidly, in contrast to those of Case a. Surprisingly, the observed TTV_{RMS} for HAT-P-13b could be well reproduced by a $\sim 2.8 M_\oplus$ super Earth near 1:1 MMR with HAT-P-13b in Case b, although RVs arose by this co-orbital perturber are larger than RMS of the RV residuals. Through over-plotting the RMS of RV residuals (RV_{RMS}) that removes the contributions from known planets, the constraints placed by RV_{RMS} are more stringent than those from TTV_{RMS} on the upper mass limits; similar simulation results have been obtained for HAT-P-16 and WASP-32 systems. As presented in panel a of Figure 12, a coplanar perturbing planet with mass of $0.011 - 0.24 M_\oplus$ initially on circular orbit would generate a TTV_{RMS} of 204.4 s when it is near 3:2 MMR with HAT-P-13b. For the perturber initially on slightly eccentric and inclined orbit, the upper mass limits near 2:1 MMR from the TTV simulation are under those of RV_{RMS} , as shown in panel c of Figure 12.

6.2.2 HAT-P-16b

The measured TTV_{RMS} of HAT-P-16b was 85.5s. In Case a, all stable orbital architectures could not reproduce the observed TTV scatter as shown in Figure 13. When hypothetical planets of $0.0037 M_\oplus$ and $1.29 M_\oplus$ reside near 1:1 and 3:1 MMRs in Case b, they can yield the observed TTV_{RMS} ; and $0.417 M_\oplus$, $0.749 M_\oplus$, $1.479 M_\oplus$ near 7:3, 5:2 and 4:1 MMRs in Case c, respectively.

6.2.3 WASP-32b

The measured TTV_{RMS} of WASP-32b was 70.8s. When hypothetical bodies of $1.0 \times 10^{-3} M_\oplus$ near the 1:1 MMR, $0.0029 M_\oplus$ near the 2:1 MMR and $0.99 M_\oplus$ near the 3:1 MMR in Case a, they could cause the observed TTV scatter. For Case b, extral planets of $0.107 M_\oplus$ and $0.759 M_\oplus$ will generate that TTV_{RMS} , when they are near 2:1 and 3:1 MMRs with WASP-32b, respectively. For Case c, the extral planets with masses of $0.536 M_\oplus$, $0.285 M_\oplus$, $0.531 M_\oplus$, $0.971 M_\oplus$ and $3.426 M_\oplus$ near 7:3, 5:2, 3:1, 4:1 and 6:1 MMRs, respectively, would well reproduced the observed TTV_{RMS} for WASP-32b. See Figure 14 for further details.

7 CONCLUSIONS

We have carried out an analysis for the transiting exoplanetary systems HAT-P-13, HAT-P-16 and WASP-32 based on new photometric data observed by TESS, OLT-1.2m, YO-1m and YO-2.4m telescopes and the data from ETD website. We employ the GP to correct the systematic errors hidden in the light curves, use the MCMC technique to model the final light curves and derive the system parameters. The refined system parameters are consistent with the previous results. We find that both HAT-P-13 b and HAT-P-16 b show significant timing variations which can be explained with apsidal precession, the timing variation of WASP-32b may be led by a decaying orbit due to tidal dissipation or apsidal precession. However, these TTVs could also be reproduced by the gravitational perturbations of close planetary companions.

ACKNOWLEDGEMENTS

We acknowledge the support of the staffs of the Hamburg 1.2m, Lijiang 2.4m and Kunming 1m telescopes. Funding for the Lijiang 2.4m telescope has been provided by Chinese Academy of Sciences and the People's Government of Yunnan Province. We appreciate the referee for his/her helpful suggestions and comments, which led to

a significant improvement to the paper. This work is supported by National Natural Science Foundation of China through grants No. U1531121, No. 10873031, No. 11473066 and No. 12003063. We also acknowledge the science research grant from the China Manned Space Project with NO. CMS-CSST-2021-B09. This paper includes data collected by the TESS mission, which is funded by the NASA Explorer Program.

This work has been conducted under the frame between China Scholarship Council (CSC) and Deutscher Akademischer Austausch Dienst (DAAD). The joint research project between Yunnan Observatories and Hamburg Observatory is funded by Sino-German Center for Research Promotion (GZ1419).

DATA AVAILABILITY

TESS data products can be accessed through the official NASA website <https://heasarc.gsfc.nasa.gov/docs/tess/data-access.html>.

The data that support the plots within this paper and other findings of this study are available from the corresponding authors upon reasonable request.

REFERENCES

- Agol E., Steffen J., Sari R., Clarkson W., 2005, *MNRAS*, **359**, 567
- Ahrer E., Wheatley P. J., Kirk J., Gandhi S., King G. W., Loudon T., 2022, *MNRAS*, **510**, 4857
- Aladağ Y., Akyüz A., Bastürk Ö., Aksaker N., Esmer E. M., Yalçinkaya S., 2021, arXiv e-prints, p. arXiv:2109.06108
- Bai L., Gu S., Wang X., Sun L., Kwok C.-T., Hui H.-K., 2022, *AJ*, **163**, 208
- Bakos G., Noyes R. W., Kovács G., Stanek K. Z., Sasselov D. D., Domsa I., 2004, *PASP*, **116**, 266
- Bakos G. Á., et al., 2009, *ApJ*, **707**, 446
- Baluev R. V., et al., 2019, *MNRAS*, **490**, 1294
- Barker A. J., Ogilvie G. I., 2010, *MNRAS*, **404**, 1849
- Batygin K., Bodenheimer P. H., Laughlin G. P., 2016, *ApJ*, **829**, 114
- Borucki W. J., et al., 2011, *ApJ*, **728**, 117
- Bouma L. G., et al., 2019, *AJ*, **157**, 217
- Bouma L. G., Winn J. N., Howard A. W., Howell S. B., Isaacson H., Knutson H., Matson R. A., 2020, *ApJ*, **893**, L29
- Brothwell R. D., et al., 2014, *MNRAS*, **440**, 3392
- Brown D. J. A., et al., 2012, *ApJ*, **760**, 139
- Buchhave L. A., et al., 2010, *ApJ*, **720**, 1118
- Buhler P. B., Knutson H. A., Batygin K., Fulton B. J., Fortney J. J., Burrows A., Wong I., 2016, *ApJ*, **821**, 26
- Carter J. A., Winn J. N., 2009, *ApJ*, **704**, 51
- Ciceri S., et al., 2013, *A&A*, **557**, A30
- Cincotta P. M., Simó C., 2000, *A&AS*, **147**, 205
- Cincotta P. M., Giordano C. M., Simó C., 2003, *Physica D Nonlinear Phenomena*, **182**, 151
- Claret A., 2000, *A&A*, **359**, 289
- Claret A., 2004, *A&A*, **428**, 1001
- Collier Cameron A., et al., 2006, *MNRAS*, **373**, 799
- Collier Cameron A., et al., 2007, *MNRAS*, **380**, 1230
- Cortés-Zuleta P., Rojo P., Wang S., Hinse T. C., Hoyer S., Sanhueza B., Correa-Amador P., Albornoz J., 2020, *A&A*, **636**, A98
- Davoudi F., et al., 2020, *New Astron.*, **76**, 101305
- Delisle J. B., 2017, *A&A*, **605**, A96
- Eastman J., Siverd R., Gaudi B. S., 2010, *PASP*, **122**, 935
- Enoch B., Collier Cameron A., Parley N. R., Hebb L., 2010, *A&A*, **516**, A33
- Espinoza N., Kossakowski D., Brahm R., 2019, *MNRAS*, **490**, 2262
- Evans T. M., Aigrain S., Gibson N., Barstow J. K., Amundsen D. S., Tremblin P., Mourier P., 2015, *MNRAS*, **451**, 680
- Fan Y.-F., Bai J.-M., Zhang J.-J., Wang C.-J., Chang L., Xin Y.-X., Zhang R.-L., 2015, *Research in Astronomy and Astrophysics*, **15**, 918
- Ford E. B., 2006, *ApJ*, **642**, 505
- Foreman-Mackey D., Hogg D. W., Lang D., Goodman J., 2013, *PASP*, **125**, 306
- Fujita N., Hori Y., Sasaki T., 2022, *ApJ*, **928**, 105
- Fulton B. J., Shporer A., Winn J. N., Holman M. J., Pál A., Gazak J. Z., 2011, *AJ*, **142**, 84
- Gaia Collaboration et al., 2021, *A&A*, **649**, A1
- Gibson N. P., Aigrain S., Roberts S., Evans T. M., Osborne M., Pont F., 2012, *MNRAS*, **419**, 2683
- Giménez A., Bastero M., 1995, *Ap&SS*, **226**, 99
- Goldreich P., Soter S., 1966, *Icarus*, **5**, 375
- Goździewski K., Bois E., Maciejewski A. J., Kiseleva-Eggleton L., 2001, *A&A*, **378**, 569
- Grauzhanina A. O., et al., 2017, in Balega Y. Y., Kudryavtsev D. O., Romanuk I. I., Yakunin I. A., eds, Vol. 510, Stars: From Collapse to Collapse. p. 376, <https://ui.adsabs.harvard.edu/abs/2017ASPC..510..376G>
- Grimm S. L., et al., 2018, *A&A*, **613**, A68
- Hardy R. A., et al., 2017, *ApJ*, **836**, 143
- Hinse T. C., Christou A. A., Alvarillos J. L. A., Goździewski K., 2010, *MNRAS*, **404**, 837
- Holczer T., et al., 2016, *ApJS*, **225**, 9
- Holman M. J., Murray N. W., 2005, *Science*, **307**, 1288
- Hurt S. A., et al., 2021, *AJ*, **161**, 157
- Jenkins J. M., et al., 2016, in Chiozzi G., Guzman J. C., eds, Society of Photo-Optical Instrumentation Engineers (SPIE) Conference Series Vol. 9913, Software and Cyberinfrastructure for Astronomy IV. p. 99133E, doi:10.1117/12.2233418
- Kramm U., Nettelmann N., Fortney J. J., Neuhäuser R., Redmer R., 2012, *A&A*, **538**, A146
- Lacedelli G., et al., 2022, *MNRAS*, **511**, 1000
- Lightcurve Collaboration et al., 2018, Lightcurve: Kepler and TESS time series analysis in Python (ascl:1812.013)
- Lithwick Y., Xie J., Wu Y., 2012, *ApJ*, **761**, 122
- Maxted P. F. L., et al., 2010, *PASP*, **122**, 1465
- Mazeh T., et al., 2013, *ApJS*, **208**, 16
- McCullough P. R., Stys J. E., Valenti J. A., Fleming S. W., Janes K. A., Heasley J. N., 2005, *PASP*, **117**, 783
- Mordasini C., 2018, Planetary Population Synthesis. p. 143, doi:10.1007/978-3-319-55333-7_143
- Mordasini C., Alibert Y., Benz W., 2009, *A&A*, **501**, 1139
- Moutou C., et al., 2011, *A&A*, **533**, A113
- Nascimbeni V., Piotto G., Bedin L. R., Damasso M., Malavolta L., Borsato L., 2011, *A&A*, **532**, A24
- Nesvorný D., Kipping D. M., Buchhave L. A., Bakos G. Á., Hartman J., Schmitt A. R., 2012, *Science*, **336**, 1133
- Nesvorný D., Chrenko O., Flock M., 2022, *ApJ*, **925**, 38
- Nesvorný D., Morbidelli A., 2008, *ApJ*, **688**, 636
- Patra K. C., Winn J. N., Holman M. J., Yu L., Deming D., Dai F., 2017, *AJ*, **154**, 4
- Payne M. J., Ford E. B., 2011, *ApJ*, **729**, 98
- Pearson K. A., Turner J. D., Sagan T. G., 2014, *New Astron.*, **27**, 102
- Pollacco D. L., et al., 2006, *PASP*, **118**, 1407
- Pál A., Sárneczky K., Szabó G. M., Szing A., Kiss L. L., Mező G., Regály Z., 2011, *MNRAS*, **413**, L43
- Rasmussen C. E., Williams C. K. I., 2006, Gaussian Processes for Machine Learning
- Rein H., Tamayo D., 2015, *MNRAS*, **452**, 376
- Rein H., Tamayo D., 2016, *MNRAS*, **459**, 2275
- Rowe J. F., et al., 2014, *ApJ*, **784**, 45
- Sada P. V., Ramón-Fox F. G., 2016, *PASP*, **128**, 024402
- Sada P. V., et al., 2012, *PASP*, **124**, 212
- Schwarz G., 1978, Annals of Statistics, **6**, 461
- Southworth J., et al., 2009, *MNRAS*, **396**, 1023
- Southworth J., Bruni I., Mancini L., Gregorio J., 2012, *MNRAS*, **420**, 2580
- Sun L.-L., et al., 2015, *Research in Astronomy and Astrophysics*, **15**, 117

- Sun L., et al., 2017, [AJ](#), **153**, 28
- Sun L., Ioannidis P., Gu S., Schmitt J. H. M. M., Wang X., Kouwenhoven M. B. N., 2019, [A&A](#), **624**, A15
- Sun L., et al., 2022, [MNRAS](#), **512**, 4604
- Szabó G. M., et al., 2010, [A&A](#), **523**, A84
- Tamuz O., Mazeh T., Zucker S., 2005, [MNRAS](#), **356**, 1466
- Tan H. B., Wang X. B., Gu S. H., Cameron A. C., 2013, *Acta Astronomica Sinica*, **54**, 527
- Turner J. D., et al., 2016, [MNRAS](#), **459**, 789
- Turner J. D., Ridden-Harper A., Jayawardhana R., 2021, [AJ](#), **161**, 72
- Valeev A. F., Grauzhanina A. O., Valyavin G. G., Galazutdinov G. A., 2019, in Kudryavtsev D. O., Romanyuk I. I., Yakunin I. A., eds, Vol. 518, *Physics of Magnetic Stars*. p. 225, <https://ui.adsabs.harvard.edu/abs/2019ASPC..518..225V>
- Wang X.-B., Gu S.-H., Li X.-J., 2010, *Earth Moon and Planets*, **106**, 97
- Wang X.-B., Gu S.-H., Collier Cameron A., Tan H.-B., Hui H.-K., Kwok C.-T., Yeung B., Leung K.-C., 2013, *Research in Astronomy and Astrophysics*, **13**, 593
- Wang X.-b., Gu S.-h., Collier Cameron A., Wang Y.-b., Hui H.-K., Kwok C.-T., Yeung B., Leung K.-C., 2014, [AJ](#), **147**, 92
- Wang Y.-H., et al., 2017, [AJ](#), **154**, 49
- Wang X.-Y., et al., 2018a, [PASP](#), **130**, 064401
- Wang S., et al., 2018b, [AJ](#), **156**, 181
- Wang C.-J., et al., 2019, *Research in Astronomy and Astrophysics*, **19**, 149
- Wang X.-Y., et al., 2021, [ApJS](#), **255**, 15
- Winn J. N., et al., 2010, [ApJ](#), **718**, 575
- Wu D.-H., Zhang R. C., Zhou J.-L., Steffen J. H., 2019, [MNRAS](#), **484**, 1538
- Xie J.-W., Wu Y., Lithwick Y., 2014, [ApJ](#), **789**, 165
- Yee S. W., et al., 2020, [ApJ](#), **888**, L5
- Zechmeister M., Kürster M., 2009, [A&A](#), **496**, 577
- Zhu W., Petrovich C., Wu Y., Dong S., Xie J., 2018, [ApJ](#), **860**, 101

This paper has been typeset from a \LaTeX file prepared by the author.